NASA Technical Paper 1769

Steady and Nonsteady Supersonic Turbulent Afterbody Flow

Kenneth K. Yoshikawa and Alan A. Wray

FEBRUARY 1981

NASA

NASA Technical Paper 1769

Steady and Nonsteady Supersonic Turbulent Afterbody Flow

Kenneth K. Yoshikawa and Alan A. Wray
Ames Research Center
Moffett Field, California

SYMBOLS

A integral quantity (eq. (A3))

c speed of sound

e total energy

F radial flux

f dependent variable

G axial flux

H step height, $R_O - R_s$; or source of radial momentum (eq. (A1))

L location of pressure sensor

M Mach number

p pressure

$[R]$ Reynolds number in a cell, $\rho_\infty U_\infty \Delta / \epsilon$

R_O base radius

R_s sting radius

R_w radius of the shock-tube wall

r radial direction

s distance from the root of the base: negative values indicate distance toward the shoulder; positive values indicate distances toward the downstream direction

T temperature

$\bar{t}$ dimensionless time, $t/(R_O/c_1)$

U free-stream velocity

u velocity in x direction

v velocity in r direction

x axial distance from the root of the base

γ specific heat ratio

Δ dimension of a cell (size of cell, total length/127)

δ increment

δ_{ij} Kronecker delta: 1 if $i = j$ and 0 if $i \neq j$

ϵ eddy viscosity

ζ ratio of the reattachment distnace for $\gamma = 1.4$ to that for other values of γ

ρ density

τ time

ω · vorticity, $\omega = -\left(\dfrac{\partial u}{\partial r} - \dfrac{\partial v}{\partial x}\right)$

$\bar{\omega}$ $\omega/(c_1/R_o)$

Subscripts:

D dividing stream line

i,j,k indexes

o base

R reattachment

W wall

∞ undisturbed free stream

1   behind the primary shock wave

2   behind the bow shock wave

STEADY AND NONSTEADY SUPERSONIC TURBULENT AFTERBODY FLOW

Kenneth K. Yoshikawa and Alan A. Wray

Ames Research Center

SUMMARY

A theoretical study of a supersonic turbulent afterbody flow field, containing regions of separation, recompression, recirculation, redevelopment, and inviscid flow, is made for axisymmetric supersonic steady and nonsteady flow past a cylindrical base supported by a sting.

The effect of the specific heat ratio γ of the incoming ideal gas on the flow properties, especially on pressure distributions along the base and sting surfaces and on reattachment distance, is investigated. The specific heat ratios considered are $\gamma = 1.2$, 1.4, and 1.667. Also, effects of other major parameters, such as eddy-viscosity coefficient (or effective Reynolds number) and Mach number, on the afterbody pressure and reattachment distance are studied and discussed. Evolution of shock-induced flow and stabilization time are examined and discussed for a transient problem.

The important influence of the flow-field geometry, pressure distributions, and reattachment distance on the aerodynamics and radiative heat transfer for an atmosphere entry probe in high-speed flight are briefly described.

INTRODUCTION

The supersonic flow over a body with a blunt trailing edge (afterbody flow) is one of the most complicated problems in fluid mechanics. It contains a rapid expansion region around the base or trailing edge, a turbulent jet mixing of the external flow with a recirculating flow at the base region, recompression process, reattachment, and finally a redevelopment region due to the trailing shock wave at the wake. Because this afterbody flow strongly influences the drag of high-speed vehicles and missiles, considerable efforts have been devoted to its understanding (refs. 1–11). More recently, two other important projects involving the study of afterbody flow have been undertaken. These are the Galileo probe to Jupiter and the MX missile placed in a long ground tunnel. It was recently found that a significant amount of the radiation heating to the Galileo entry probe comes from the highly recompressed gas radiation from the wake region; this is in addition to the well-known radiant heating to the forebody surface (refs. 12–17). Thus, the design of the heat shield for the base of this vehicle requires a thorough understanding of the wake-flow structure from the near-wake to the far-wake regions. In the MX missile problem, the characteristics of the blast-induced shock wave and its interaction with the ground tunnel affect the survivability of the missile (ref. 18). This problem also involves the nonsteady turbulent flow over the missile, including the wall interference with the primary and secondary bow shock waves.

Reviews of various methods of analysis applicable to the wake-flow regions have been presented in references 10 and 11. Analytical methods using integral approaches (refs. 1, 2) and

empirical models based on detailed experimental data (ref. 7) have been proposed previously. Recently, mathematical turbulence models have been reviewed in detail in reference 19. The turbulence models, however, are still not well understood. A simple model (of constant viscosity, constant Prandtl number, $Pr = 1$, and constant γ) is desirable to simplify the computations; one such model has been previously introduced to solve the *laminar* near-wake-flow problem with some success (refs. 4, 5).

Major emphasis in this report is on the development of a simple analytical method for studying the *turbulent* afterbody flow problem. A simple model, using an appropriate value of eddy viscosity and ideal gas, is employed for the fully developed turbulent flow calculations. This simple model will be particularly useful in providing some physical insight into the problem, for example, by examining the numerical effect of eddy viscosity (or effective Reynolds number) and specific heat ratio γ on the flow field.

NUMERICAL FLOW SIMULATION

Steady Flow

A schematic of the afterbody flow is shown in figure 1. The afterbody flow field consists of several distinct regions and processes: The supersonic flow, assumed uniform at the corner (with a thin boundary layer) at Mach number M_1, expands rapidly and separates around the edge of the base, forms a free shear layer, and goes through a constant-pressure jet mixing, recompression, and reattachment; it then goes through a compression shock wave and redevelopment process. A portion of the shear-layer fluid is trapped in the base region and creates a recirculating flow bounded by a dividing streamline, the base wall, and sting surface; the rest of the viscous flow proceeds in far-wake direction.
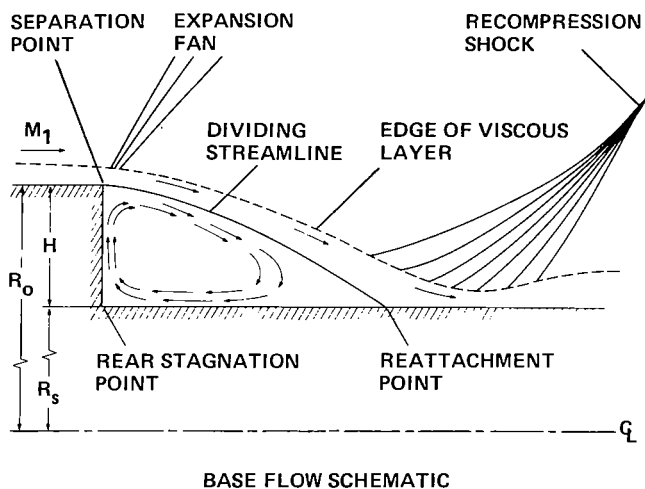
To evaluate steady-state flow, two computer codes, the Weng-Chow code (ref. 1) and Wray's code (ref. 20), were used, and some of their significant results are compared. Note that the Weng-Chow code has a more realistic turbulence model, but its solution is limited to flow in the recirculation region; on the other hand, Wray's model is primitive (though it can be modified), but its solution covers the entire flow region. Of the various fluid dynamics properties (pressure, density, temperature, velocity, vorticity, etc.), the pressure distribution is especially informative at hypersonic speeds since it is mainly dependent on velocity and less so on the other fluid properties and physical parameters. These codes are briefly described below.

Figure 1.— Separation and recompression regions of axisymmetric flow over a cylindrical step base.

In the Weng-Chow code, the methods of analysis and calculation for various flow properties in the corner, turbulent jet mixing, recompression, reattachment, and redevelopment regions are obtained by the integral method described in detail in references 1 and 2. The inviscid flow region is described using the method of characteristics. The Prandtl mixing-length theory is used to compute the turbulent shear stress in the free mixing layer under a constant-pressure assumption. A spatial variation of eddy viscosity — in which the eddy viscosity is proportional to the value at the end of the mixing region times the local velocity scale and to the seventh power of the distance from the mixing region — was employed in the region of recompression. Solutions are obtained by cut-and-trial, adjusting some of the major parameters between trials. (The program was loaned to Ames Research Center by Professor W. L. Chow, University of Illinois.) The calculation of wall-pressure distribution along the sting surface was reported to show good agreement with experimental data, except that the computed peak pressures were generally higher and the gradients much steeper than experimental values (refs. 1, 2).

Wray's code is a computational code for afterbody flow, using the compressible Reynolds-averaged, Navier-Stokes equations; it is an explicit method that is second-order accurate in space and time (unsplit, Richtmyer and Morton method). A brief derivation and description of the method are given in the appendix. A steady-state condition is reached in about 10,000 steps; it requires about 20 min on the ILLIAC IV. The computational domain considered is about 4 times the body radius in the radial direction and about 6.5 times the body radius in the streamwise direction. Emphasis is on constructing the overall flow field around the afterbody. An adiabatic base and sting (and slip-flow condition for the shock-tube wall when wall interaction is considered) are used. A simple physical model has been incorporated in the calculations to determine the qualitative effects of the parameters on the flow-field solutions; the model consists of an ideal gas (constant γ), constant eddy viscosity, and unit Prandtl number ($Pr = 1$).
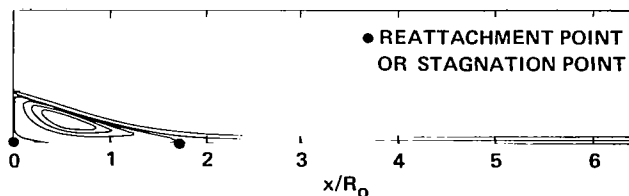
The essential features and results of the present calculations, using Wray's code, are described in the following sections and are shown in figures 2–6.

Effect of cell Reynolds number— The effect of cell Reynolds number $[R]$, or inverse dimensionless eddy viscosity, on the flow field is shown in figures 2 and 3. Shown in figure 2 are computed pressure contours and streamlines in the afterbody region. Conditions for this case are $[R] = 100$, $\gamma = 1.2$, $M_1 = 2.38$, and $R_S/R_O = 1/2$.

Conical expansion and recompression waves can be clearly identified in figure 2(a). There are large constant-pressure regions behind the cylindrical base and downstream of the recompression shock wave. The slight variation of the pressure
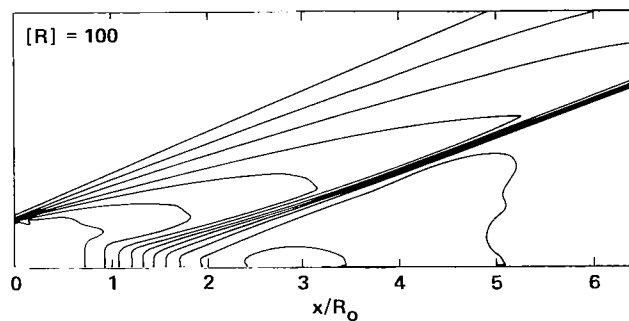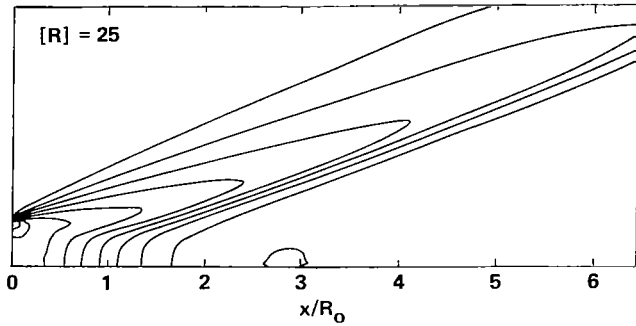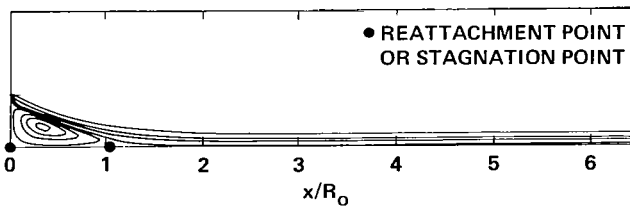

(a) Pressure contours.

(b) Stream lines, exponential spacing.

Figure 2.— Afterbody flow solution: $M_1 = 2.38$, $R_S/R_O = 1/2$, $[R] = 100$, and $\gamma = 1.2$.
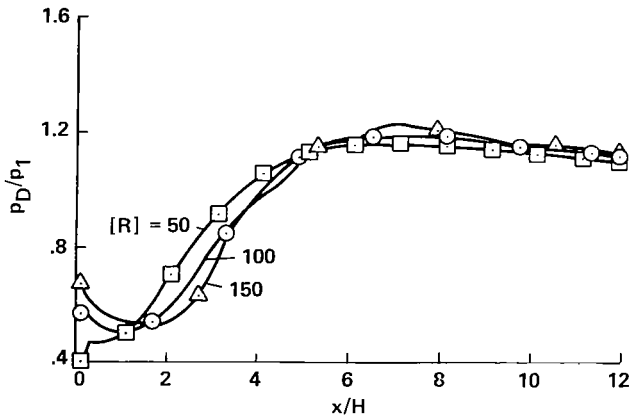
3

(a) Pressure contours.

• REATTACHMENT POINT
OR STAGNATION POINT

(b) Stream function, exp (ψ).

Figure 3.– Afterbody flow solution: $M_1 = 2.38$, $R_s/R_O = 1/2$, [R] = 25, and $\gamma = 1.2$.

(a) The effect of [R] on pressure distribution along dividing stream line: $M_1 = 2.09$, $\gamma = 1.67$, $R_s/R_O \cong 1/2$.

Figure 4.– Pressure distributions.

between the base and the recompression shock indicates a possibility of boundary-layer-like flow in that region. The pressure distribution along the sting surface shows that the pressure buildup is gradual; after the peak value is reached, the pressure decreases very slowly to the free-stream value. Shown in figure 2(b) are streamlines (with exponential spacing); a pattern of the recirculatory flow as well as the dividing streamline through the rear stagnation point (reattachment points are marked by circular symbols) can be seen.

Pressure contours and streamlines for a larger eddy viscosity ([R] = 25) are shown in figure 3 for the same values of γ, M_1, and R_s/R_O as used in the previous case. The base pressure below the corner is drastically reduced (fig. 3(a)). Strong vorticity and turbulence carry momentum around the corner and delay the boundary-layer separation, that is, separation occurs below the corner, decreasing the size of the wake and the reattachment distance, as can be seen from figure 3(b). This delay of boundary-layer separation has been observed in numerous experimental investigations (e.g., ref. 9). Some numerical analyses for laminar two-dimensional flow behind a wedge or step (refs. 4, 5) also pointed out this behavior. The separation delay will be discussed further in a following subsection (Vorticity Distribution). The steep pressure gradient near the corner suggests that the boundary-layer character of the flow along the corner vanishes as the flow expands. These results simply indicate the influence of larger eddy viscosity. In our report, however, for simplicity we assume a constant eddy viscosity.

The effect of [R] on pressure distributions is shown in figures 4–6. Pressure distributions on the dividing streamline, particularly in the vicinity of the corner, vary significantly with the value of [R], as shown in figure 4(a). The results for other values of γ show pressure variations similar to those

for $\gamma = 1.67$. Note that the pressure distribution along the sting surface (p_W) does not vary as much with $[R]$ as that along the dividing streamline (p_D). Also note that a steep pressure gradient appears near the corner for the small value of $[R]$; this is also clearly shown in figure 3(a).

The concept of constant-pressure mixing, after the flow separation, has been supported by many authors for lower supersonic speeds, that is, $M_1 < 3$ (e.g., refs. 1–6, 10, 11, 13). In order to obtain relatively constant pressure p_D in the base mixing region and also to keep the base pressure close to this pressure (i.e., $p_B \cong p_D$), an appropriate value of $[R]$ has to be selected. The value that satisfies these conditions is $[R] \approx 75$. Pressure distributions of p_D and p_W for $[R] = 75$ are shown in figure 4(b) where, as can be seen, p_D in the turbulent jet mixing layer is nearly constant from $x/H = 0$ to $x/H \approx 2.0$, ahead of the reattachment point, and is also nearly equal to the base pressure (note that p_D becomes identical to p_W after flow reattachment).

The numerical calculations for other values of γ (i.e., $\gamma = 1.2$ and 1.4) show similar results and, thus, support the choice of $[R] \cong 75$. Presented in figure 4(c) are pressure distributions for a higher Mach number $(M_1 = 4)$. The numerical results show that the effect of $[R]$ on pressure distributions is relatively small for higher Mach numbers, but is somewhat larger for lower Mach numbers. Thus, base pressure is weakly dependent on $[R]$ (see also refs. 1, 10). It is also noted that pressure varies rapidly along the dividing streamline and that constant-pressure mixing can no longer exist in this high-shear flow region for higher Mach number. Note that the feature of constant wall pressure (below the separation point) still exists in the base flow region.

In figure 4(c) negative values on the abscissa indicate locations between the corner $(s/H = -1)$ and the root of the base $(s/H = 0)$.

Effect of specific heat ratio— For hypersonic entry into a planetary atmosphere it is known that the specific heat ratio of the high-temperature real gas will change significantly during the flight; therefore, the examination of the effect of γ on the flow field is important. Three different
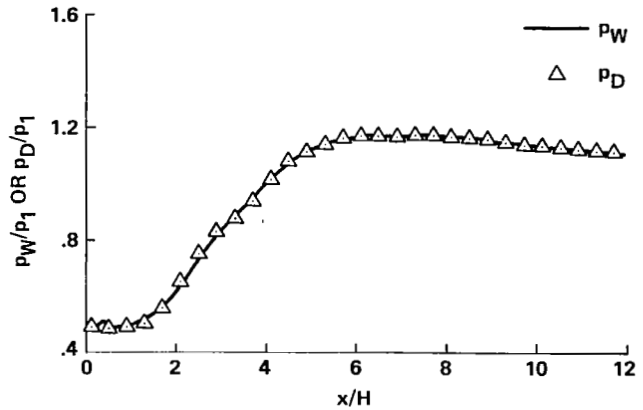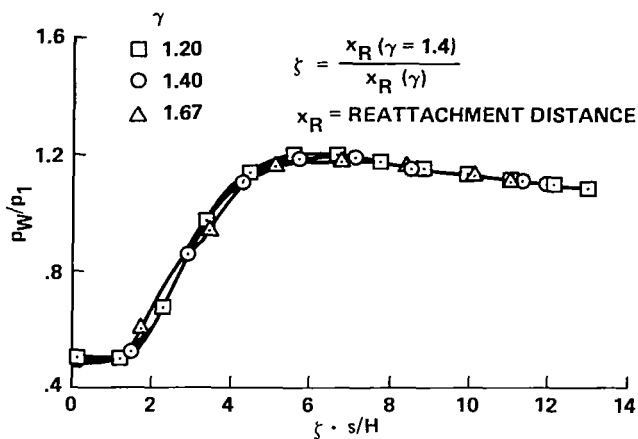
(b) Pressure distributions for the effective $[R] = 75$. $M_1 = 2.09, \gamma = 1.67, R_s/R_o \cong 1/2$.
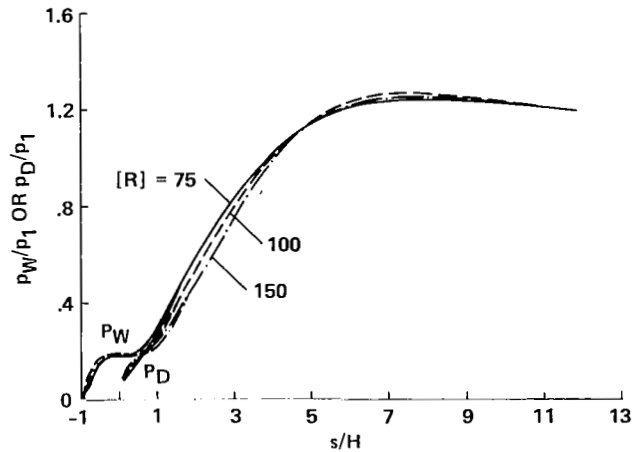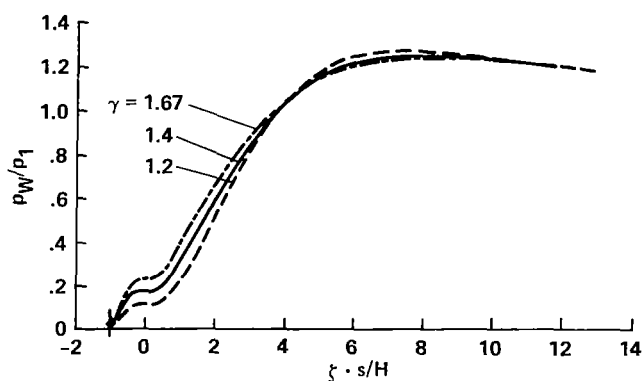
(c) The effect of $[R]$ on pressure distributions at higher Mach number. $M_1 = 4.0, \gamma = 1.4, R_s/R_o \cong 1/2$.

Figure 4.– Concluded.

$$\zeta = \frac{x_R\,(\gamma = 1.4)}{x_R\,(\gamma)}$$

γ
□ 1.20
○ 1.40
△ 1.67

x_R = REATTACHMENT DISTANCE

(a) $M_1 = 2.09$, $R_s/R_O = 1/2$, and $[R] = 75$.

$\gamma = 1.67$
1.4
1.2

(b) $M_1 = 4.0$, $[R] = 75$, and $R_s/R_O = 1/2$.

Figure 5.— The effect of γ on pressure distributions.

values of constant γ are used in the calculations in order to see the effect of γ on the pressure distributions.

A rather good correlation of pressure distributions for $\gamma = 1.2$, 1.4, and 1.67 is obtained in the form of a reduced coordinate, as shown in figure 5(a). The flow conditions for the cases are $M_1 = 2.09$ and $R_s/R_O = 1/2$. The factor ζ in the abscissa is the ratio of the reattachment distance for $\gamma = 1.4$ to that for a given γ. Experimental correlation of pressure distributions in the reduced form have been demonstrated in reference 6 for air, and seem valid for a reasonable range of R_s/R_O. The detailed effect of the ratio of the sting radius to the body radius, R_s/R_O, on the pressure distributions and reattachment distance are shown in references 1 and 8, based on theory and experiments in air. It should be noted here that significant overshoot pressure, following the flow reattachment, is observed for axisymmetric flow (see also fig. 4), but no overshoot is seen in two-dimensional flow (refs. 6, 8).

The effect of γ on the pressure distribution at a higher Mach number, $M_1 = 4.0$, is shown in figure 5(b). The results clearly indicate that the base pressure is strongly dependent on both flow Mach number M_1 and specific heat ratio of the gas γ, that is, the base pressure ratio is significantly reduced by increasing M_1 and by decreasing γ. The maximum pressure ratio, p_{max}/p_1, however, is relatively independent of these parameters (p_{max}/p_1 slightly increases as M_1 increases). Consequently, pressure distributions in the reduced coordinate do not show as good a correlation as for the lower Mach number case in the region of near-wake, but retain good correlation in the far-wake region. In figure 5 negative abscissa values indicate the locations from the corner ($s/H = -1$) to the root of the base ($s/H = 0$).

Vorticity distributions— Vorticity is plotted in reduced coordinate in figure 6 for the higher Mach number condition. The vorticity along the dividing stream line (ω_D) and along the base-to-sting surface (ω_W) is presented. Vorticity is large around the corner. Three zero vorticity points ($\omega = 0$), one just below the corner (an evidence of the delayed separation point), one at the base (rear stagnation point), and one at the flow reattachment location are present. Note that the vorticity ω_D in figure 6 should start from the origin, that is, $\omega_D = 0$ at $s = 0$. The vorticity distributions, ω_D and ω_W, become identical after flow reattachment. In contrast to the pressure distributions in figure 5(b), good correlations of the vorticity distributions exist in the region of recirculation of near-wake flow. The vorticity along the sting and base surface is positive inside the recirculation region, corresponding to reverse flow; along the dividing stream line outside the recirculation region (along the surface before the separation and after the reattachment) it is negative, corresponding to

flow in a streamwise direction. Note that strong vorticity is regenerated as the flow moves past the reattachment point.

Other general physical results are described in the following section — General Results and Discussions.

Nonsteady Flow

A shock tube is a useful facility for the experimental study of high-speed entry gas dynamics (ref. 21). In particular, shock-wave interaction with walls and projectiles inside a shock tube or in a long ground tunnel is an important subject of investigation for heat protection and safeguarding of space vehicles and missiles (ref. 18). Numerous reports have presented various features of numerical calculations for the inviscid shock-induced flow, that is, supersonic wake flow (ref. 22), shock-wave interaction with the cross-flow (ref. 23), and flow patterns of diffracting weak shock waves around corners (ref. 24). The important nonsteady flow characteristics associated with a shock-tube test, such as actual test time, flow stability time, and flow reflection time, are not well understood, except that the reflection time (time for the shock wave to travel to the end wall and return) is *usually* much longer than the test time. In this section the effects of turbulent flow on the transient pressure, flow stability time, and some effects of γ on the pressure distribution in the shock-tube flow will be briefly described.

Shock-wave-induced base flow— A sketch of the initial shock wave passing over a sting-supported cylindrical base is shown in figure 7. The primary shock wave at Mach number M_∞ diffracts at the corner and passes to the sting surface, developing the turbulent shear layers. The principal results for the transient phase of flow, from nonsteady to steady-state conditions, are shown in figure 8 for the condition of $M_\infty = 6$, $\gamma = 1.4$, and $R_s/R_O = 1/3$. Figure 8(a) shows the density contours and pressure distribution along the sting surface shortly after collision of the diffracted shock wave with the base line ($\bar{t} = 0.37$) and after collision with the sting surface ($\bar{t} = 0.74$). The pressure distribution at $\bar{t} = 0.37$ is still undisturbed, since the shock-wave front has not reached the bottom of the base surface (or sting surface). Strong overshoot pressure, due to shock wave reflection or diffraction, develops immediately and reaches a maximum value
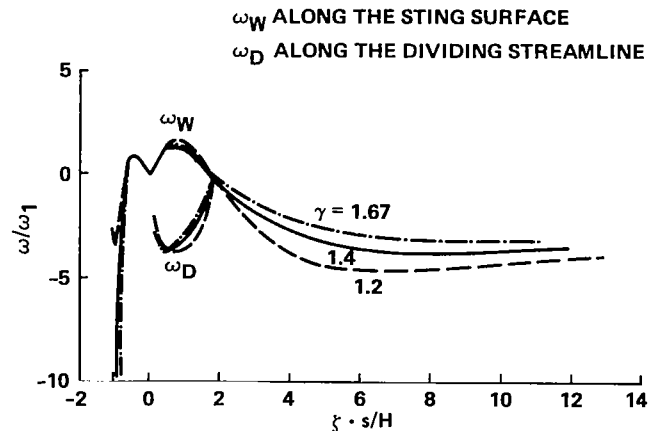

Figure 6.— The effect of γ on vorticity distributions: $M_1 = 4.0$, $[R] = 75$, and $R_s/R_O = 1/2$.
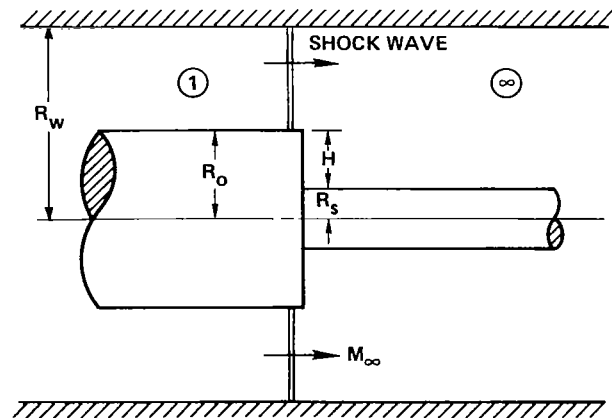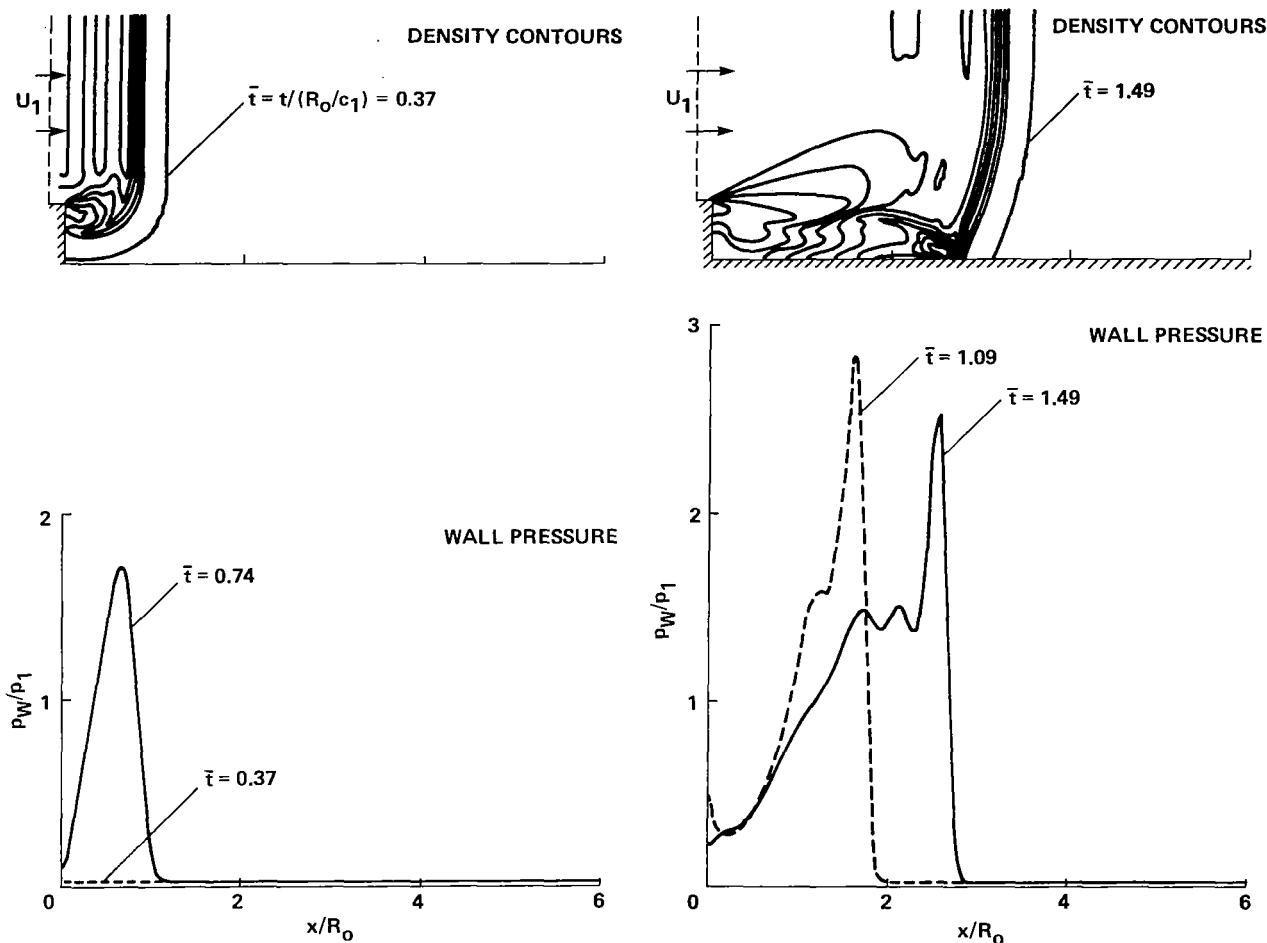

Figure 7.— Geometry of shock wave passing over a cylindrical step base supported by sting.

DENSITY CONTOURS

U_1

$\bar{t} = t/(R_0/c_1) = 0.37$

DENSITY CONTOURS

U_1

$\bar{t} = 1.49$

WALL PRESSURE

$\bar{t} = 1.09$

$\bar{t} = 1.49$

WALL PRESSURE

$\bar{t} = 0.74$

$\bar{t} = 0.37$

p_W/p_1

x/R_0

p_W/p_1

x/R_0

(a) Density contours at $\bar{t}$ = 0.37;
wall pressure at $\bar{t}$ = 0.74 and 0.37.

(b) Density contours at $\bar{t}$ = 1.49;
wall pressure at $\bar{t}$ = 1.09 and 1.49.

Figure 8.— Evolution of density and pressure distributions for shock-induced base flow:
$M_\infty = 6, R_S/R_O = 1/3, [R] = 75$, and $\gamma = 1.4$.

of $p/p_1 \approx 2.9$ (where p_1 is the pressure behind the incident shock) at $\bar{t}$ = 1.0, as shown in the subsequent figures. The major portions of flow field follow the inviscid flow character following the conical expansion around the corner, until flow time reaches $\bar{t}$ = 1.0; no significant damping or fluctuation due to viscous effects appears in the pressure distributions (see e.g., refs. 22, 23). Strong vorticity is generated as the shock moves past the corner. The starting vortex moves downstream, and its interaction with the sting becomes important, as can be seen in figure 6.

The maximum pressure buildup behind the shock occurs at a characteristic time at $\bar{t}$ = 1.0 without regard to the gas property (or γ) used in the numerical calculations. Radiant luminosity believed to be due to this peak pressure has been observed in reference 15.

Flow stability time— The base pressure ratio (p/p_1 at x/R_O = 0.0) also varies with time; this effect can be seen in figure 8. Time history of the base pressure in terms of the reduced time is

shown in figure 9. The first pressure peak (impact pressure) occurs immediately after the diffracted shock wave impinges upon the sting surface at the bottom of the base, and the base pressure then builds up again, with some fluctuations, to the asymptotic value. We arbitrarily define flow stability time τ by

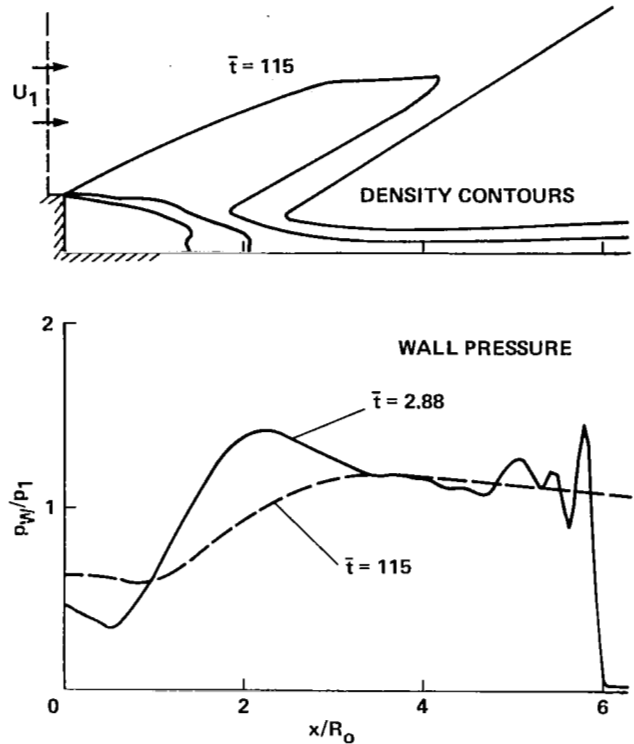$$p_B(\tau)/p_B(\infty) \equiv 0.90 \qquad (1)$$

From several numerical calculations, the following empirical relation is established for the case of $R_s/R_o = 1/3$,

$$\tau \cong 61 \cdot (R_o/c_1)/(\rho_1/\rho_\infty) \qquad (2)$$

The flow stability time will be dependent on the ratio of the sting radius to the body radius, R_s/R_o; it will be shorter when R_s/R_o is smaller since interaction with the boundary layer is less.

It is possible that the flow stability time given by equation (2) can be longer than the actual flow test time, since the flow test time can be significantly shortened by the shock-tube boundary layer growth and by the broadening of the mixing regions across the contact surface in hypersonic shock tube. It is possible that the steady-state flow may not be established in many test cases.

(c) Density contours at $\bar{t} = 115$; wall pressure at $\bar{t} = 2.88$ and 115.

Figure 8.– Concluded.

Shock-tube flow simulations– Typical results of the shock-tube flow simulation ($\bar{t} \gg 1$) are shown in figure 10. The pressure distributions along the sting surface are plotted in this figure for three different gases (i.e., $\gamma = 1.2$, 1.4, and 1.67) for $M_\infty = 14.0$ and $R_s/R_o = 1/3$. The large differences in base pressure ratios are due to the different values of the specific heat ratio γ, which also result in different flow Mach numbers M_1 ($M_1 = 2.80$, 1.86, and 1.33 for $\gamma = 1.2$, 1.4, and 1.67, respectively); however, the peak pressure ratio p_{max}/p_1 does not change significantly. The rapid pressure decay shown for a monatomic gas ($\gamma = 1.67$) is due to shock-tube wall interaction (reflection of the expansion wave from the shock-tube wall), a result of the lower supersonic speed of $M_1 = 1.33$. The wall-interaction effect on pressure for other gases ($\gamma = 1.2$ and 1.4) would appear further downstream; it cannot be seen in these figures because the Mach numbers M_1 are too high. Validity of the concept of constant-pressure mixing in the recirculation region (below the separation point) for various γ and Mach numbers M_1 is well substantiated in the figure, that is, the constant-pressure mixing and constant base-pressure assumptions seem to be valid for $\gamma \geqslant 1.2$ or for $M_1 \leqslant 3.0$.
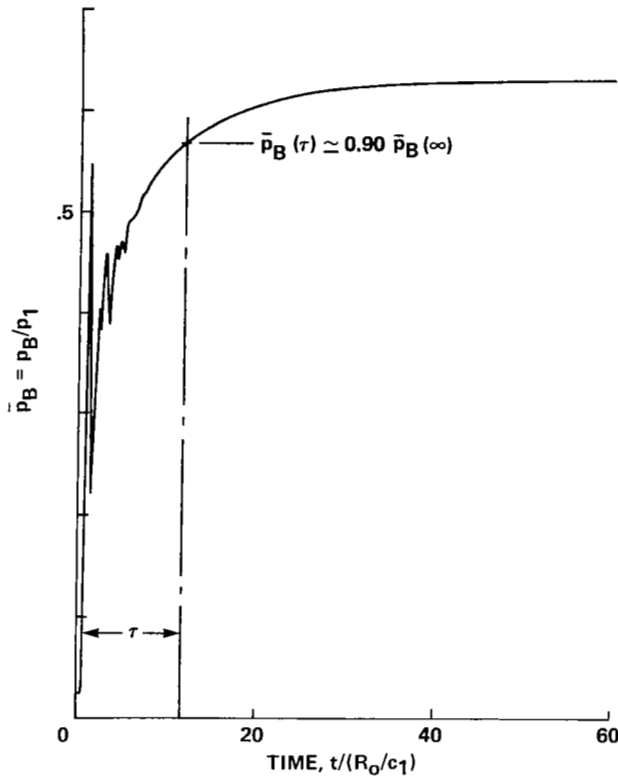
9

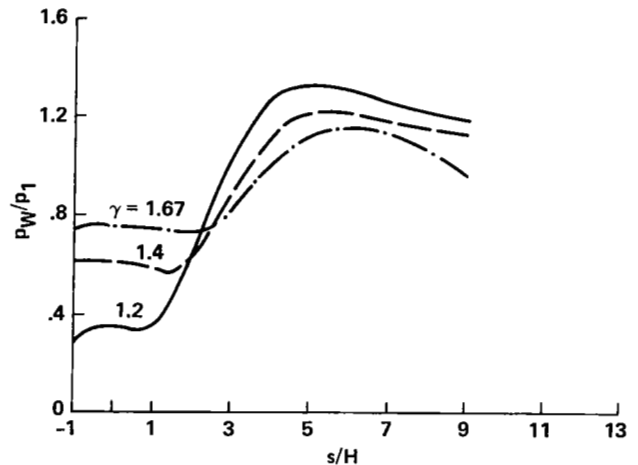Figure 9.– Transient base pressure and flow stability time: boundary conditions same as in figure 8.

Figure 10.– Pressure distributions and wall interference (shock-tube flow simulation): $M_\infty = 14$, $R_s/R_O \cong 1/3$, and $R_W/R_O \cong 4$.

GENERAL RESULTS AND DISCUSSIONS

Important physical results, such as the ratio of the neck pressure (maximum pressure) to the base pressure, p_{max}/p_1, and reattachment distance x_R, are presented and discussed in this section. (Note that $p_{max}/p_1 = (p_{max}/p_B) \cdot (p_B/p_1)$.)

Comparison of the Ratio of Base Pressure to Neck Pressure

This pressure ratio is important in the estimation of the magnitude of radiation heat from the wake (see, e.g., refs. 15, 16). The computed peak-to-base (or neck-to-base) pressure ratios are shown in figure 11(a). Since the range of sting-to-body radius ratio in this report is limited to $R_s/R_O = 0.33$ and 0.5, the radius effect on base pressure is relatively minor. Significant effect of flow Mach number and γ on p_{max}/p_1 is noted as M_1 exceeds 3.0. One can, therefore, expect very high pressure ratios for the hypersonic flow where dissociation and ionization of the gas begins to take place, that is, for a gas of low γ. Also shown in the same figure, with solid black symbols, are the results obtained by using the code of reference 1. An empirical relation derived for $\gamma = 1.4$ is presented in the figure as a dotted line, which agrees well with the results of reference 1.

10
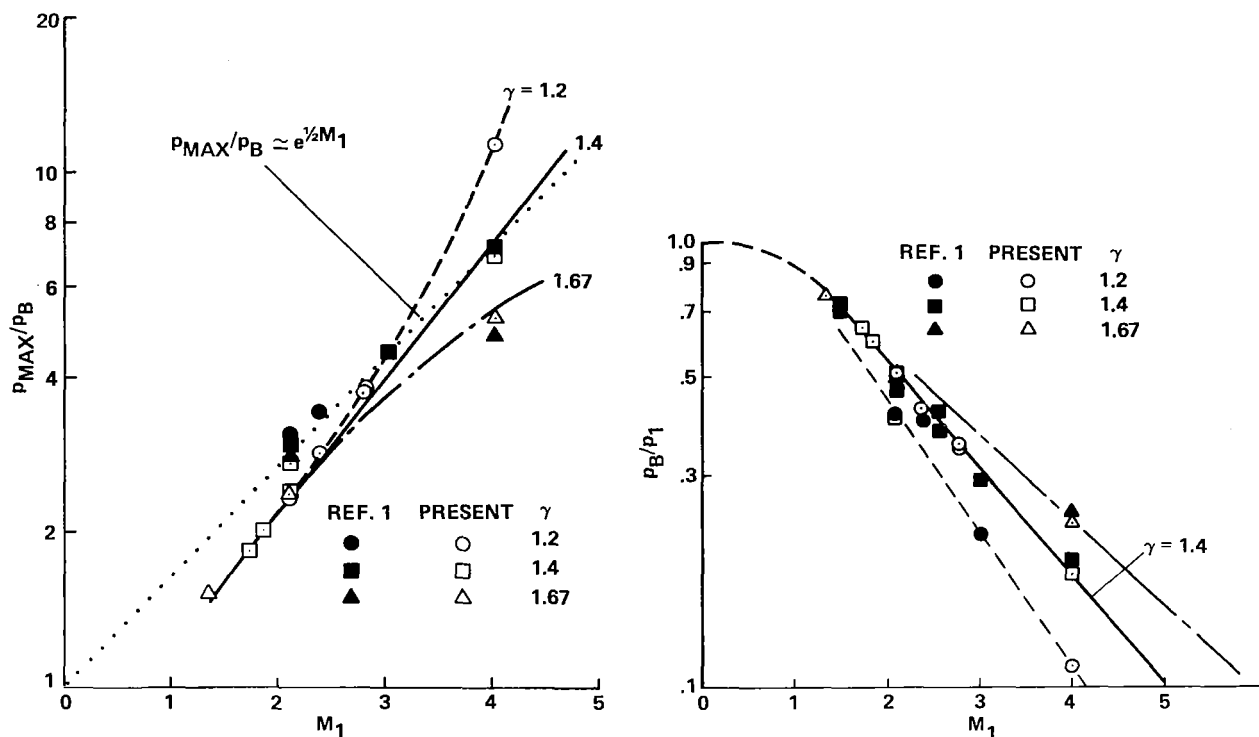
(a) Ratio of peak pressure to base pressure
as a function of Mach number.

(b) Base pressure as a function of
Mach number.

Figure 11.— Wake pressures.

Base Pressure

Base pressure ratios, p_B/p_1, calculated by the present code and by that of reference 1, are shown in figure 11(b) (numerous experimental and theoretical data are also presented in ref. 7). Significant effects of γ on the ratio is noticed as Mach number M_1 increases. The large effect of γ on the peak pressure ratio shown in figure 11(a) is due mainly to the effect of γ on base pressure since p_{max}/p_1 is relatively unchanged (see figs. 4, 5). The result shows that base pressure will be significantly lower when γ is lower, that is, when dissociation or ionization takes place in hypersonic flight. Note that the ratio of sting radius to body radius is also limited to $R_s/R_o = 0.33$ and 0.5 in the figure (the effect of body radius on base pressure, as mentioned before, is demonstrated in references 1 and 8 for lower supersonic Mach number).

Reattachment Distance

Reattachment distance of the afterbody, shown in figure 12, is an important characteristic length. It provides an approximate location of the vertex of recompression shock and, thus, gives an appropriate view factor for the wake radiation involved with the high-temperature gas. Also shown in the figure is an empirical relation for the reattachment distance for $\gamma = 1.4$. A few computed
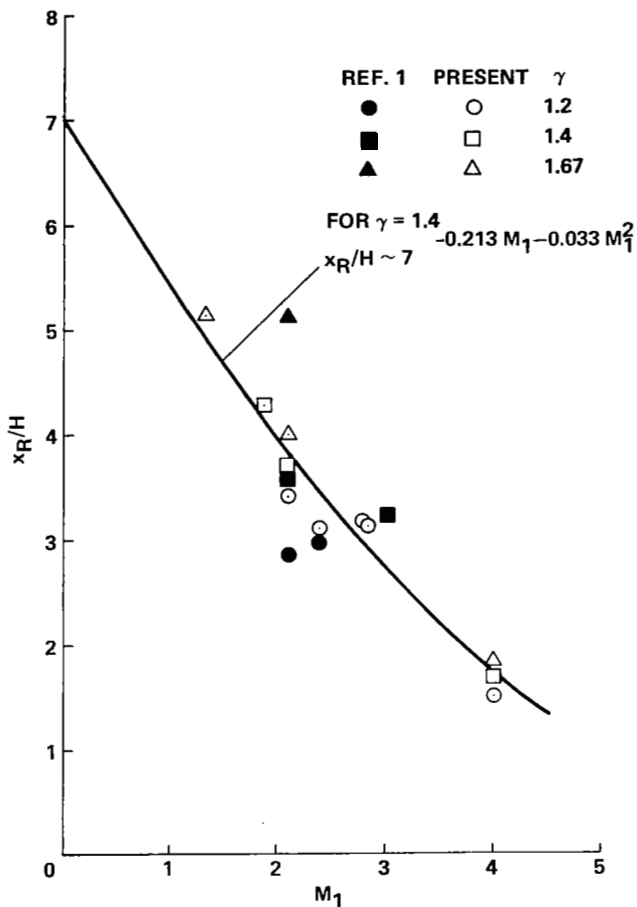
Figure 12.— Flow reattachment distance as a function of Mach number.

results from reference 1 are also included in figure 12, but the results show strong dependence on γ and fluctuate with a wide variation (the method, however, is not expected to be applicable for higher Mach numbers). The present results indicate rather good correlation, whereas those from reference 1 do not.

Forebody Flow Effect

The presence of a forebody with accompanying bow shock wave may significantly affect the afterbody flow solution. For example, the trend of experimental pressure distributions downstream of the separation point for various forebody shapes (and sting radius to body radius ratio) has been shown in references 6 and 8: distinct overshoot pressure, as shown in previous figures, results for the long cylindrical base flow, and no significant overshoot pressure is reported for the particular forebody presented. Note also that the result of two-dimensional flow (or $R_s/R_o \cong 1.0$) does not show the overshoot pressure. The detailed study of the forebody effect on the afterbody flow is, therefore, desirable. There are a number of time-dependent finite-difference Navier-Stokes codes that have been developed to calculate the turbulent viscous flow over a blunt forebody at supersonic or transonic speeds (e.g., refs. 25, 26). These codes can be incorporated with the present afterbody code in order to see the effect of a forebody.

Code Limitation

Besides the flow-model limitations mentioned earlier (i.e., ideal gas, constant turbulent eddy viscosity, etc.), there is another code limitation. Solution of the shock-induced flow (nonsteady shock-tube flow and steady wind-tunnel afterbody flow) involves a steep pressure jump across the shock wave (including the recompression shock wave). These discontinuities often cause numerical problems. The relatively gradual pressure rise across the recompression shock wave shown in figure 4, and across the diffracted shock wave shown in figure 8, can be attributed to this code limitation. (However, higher eddy viscosity also causes a gradual pressure rise.) For example, pressure distributions calculated by the code of reference 1 show much steeper pressure rises than the present results at the beginning of the recompression region, and the experiments seem to support the results of reference 1, except that the later portion of the experimental pressure rise is much more

gradual than that predicted by reference 1. Therefore, further examination and improvement on this subject may be essential.

Shock-Tube Experiments

To demonstrate the general trend of unsteady afterbody flow, a typical result of a shock-tube experiment for transient pressure distribution is shown in figure 13. The test model is a hemispherical body supported by a sting, with a ratio of sting radius to body radius of $R_S/R_O = 1/3$; the test gas is air at a shock-wave Mach number of about $M_\infty = 14$. As noted in the previous section, the forebody shape alters afterbody pressure distributions, especially after the reattachment point, and for the demonstration purpose we choose transient pressure near the base $(x/H = 1.0)$, which seems to be less affected. Air at this test condition is partially dissociated, and two numerical calculations (one for $\gamma = 1.2$ and the other for $\gamma = 1.4$) are shown for the comparison. After a sharp pressure spike, due to the diffracted shock wave compressing and interacting with the boundary layer near the surface, the transient pressure gradually increases toward the asymptotic values of p_1, the steady-state pressure behind the primary shock wave. In this test condition we estimated that the experiment test time (300–400 μsec) and the flow stability time ($\tau = 300$ μsec for $\gamma = 1.4$, and $\tau = 400$ μsec for $\gamma = 1.2$) were comparable. However, it could be that the flow does not reach the steady-state condition before the mixing region of the interface arrives at the location of the pressure sensor. Note again that the numerical calculation of transient pressure is based on the infinitely long forebody and thin-boundary-layer assumptions; agreement of the test data and numerical calculations is not emphasized here.

The extremely strong and nonsteady pressure induced by the blast shock
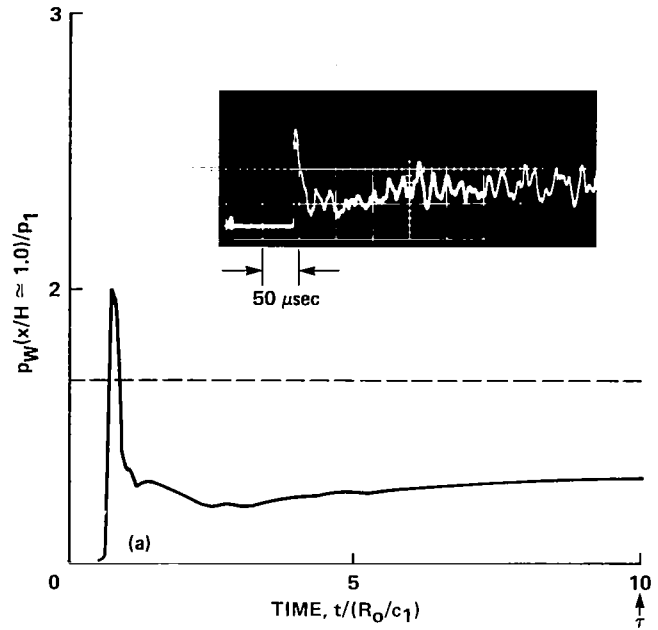
(a) $\gamma = 1.2$.
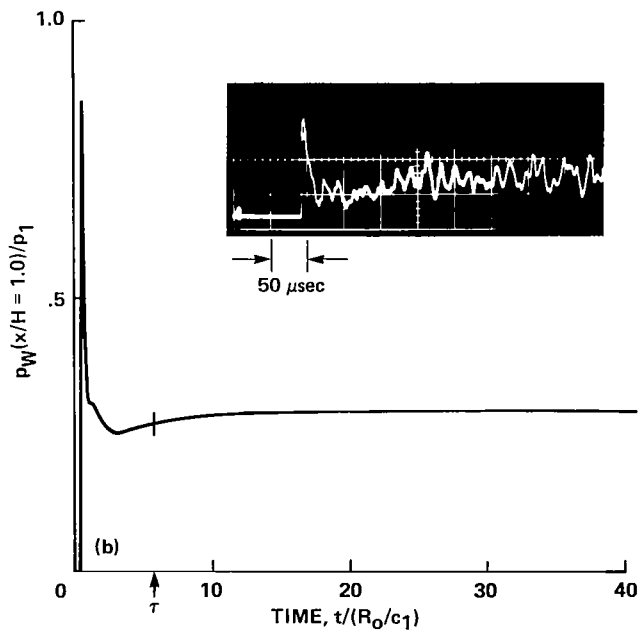
(b) $\gamma = 1.4$.

Figure 13.– Experimental and theoretical transient pressure: $M_\infty = 14$, and $R_S/R_O = 1/3$.

13

wave, which hammers the body and thus affects stability and safety of the vehicle, should be noted.

CONCLUDING REMARKS

A computer code and solutions of steady and nonsteady supersonic turbulent-wake flow have been obtained under simple flow model assumptions. The emphasis of the study was on examining the basic characteristics of the afterbody flow field to obtain essential flow information for the calculation of radiation heat from the wake region. Solution of the entire afterbody flow covered the base through far-wake regions; within the framework of the present assumptions, the solution results in the following general conclusions:

1. There is a steep pressure jump (thus, high temperature jump) across the recompression shock wave (which can be correlated for low Mach numbers, $M_1 \leqslant 3$).

2. Relatively large constant-pressure zones exist.

3. There is a gradual decay of the pressure distribution in the far-wake region (thus, slow decay of temperature and radiation intensity).

4. A conical shape of high-pressure zones (thus, high-temperature radiation sources) is an appropriate geometry for calculating radiation heat from the wake region.

For nonsteady flow, the following results are noted:

1. There is a very high induced pressure on the sting surface, which is also substantiated by experiments (several times higher than p_1, steady-state pressure behind the incident shock wave).

2. Delayed separation, rear-stagnation, and reattachment points can be identified by the vorticity distribution curve.

3. Flow stability time may be comparable with flow test time.

However, further examination of the wake flow — using improved models that include, for example, the effects of real gases, variable turbulent viscosity, presence of forebody flow, and improved resolution across shock waves — is essential to the accurate prediction of radiation heat and heat protection of a very high speed entry probe, such as that for the Galileo mission to Jupiter.

Ames Research Center
    National Aeronautics and Space Administration
        Moffett Field, California 94035, July 23, 1980

APPENDIX

DESCRIPTION OF WRAY'S CODE

The Wray code solves the Navier-Stokes equations in an axisymmetric geometry by means of a finite-difference algorithm of second-order accuracy in space and time for the inviscid terms and second-order accuracy in space and first-order accuracy in time for the viscous and heat conduction terms (ref. 20). The method of differencing enforces exact numerical conservation of mass, momentum, energy, and angular momentum.

We can write the Navier-Stokes equations in the following shorthand notation:

$$\frac{\partial f_i}{\partial t} = \frac{1}{r}\frac{\partial F_i}{\partial r} + \frac{\partial G_i}{\partial x} + H\delta_{i3} \tag{A1}$$

where $f_i = (\rho, e, \rho u, \rho v)$ is an array of the dependent variables: mass density, total energy density, radial momentum density, and axial momentum density. F_i and G_i are the corresponding radial and axial flux densities. The term H, which occurs only in the radial momentum equation, constitutes a source of radial momentum due to geometric effects in the axisymmetric coordinate system. The operator δ_{i3} is the Kronecker delta ($\delta_{i3} = 1$ if $i = 3$, zero otherwise).

We take node points $r_j = (j - 1)\,\delta r$ and $x_k = (k - 1)\,\delta x$, $j, k = 1, 2, \ldots, 128$, to represent the flow field. The values of the f_i at (r_j, x_k) are considered to be average values in a cell. We integrate (A1) to find these averages:

$$\frac{1}{A}\frac{\partial}{\partial t}\int_{r_j-(1/2)\delta r}^{r_j+(1/2)\delta r}\int_{x-(1/2)\delta x}^{x+(1/2)\delta x} f_i r\, dr\, dx$$

$$= \frac{1}{A}\int_{x_k-(1/2)\delta x}^{x_k+(1/2)\delta x}\left[F_i\left(r_j+\frac{1}{2}\delta r\right) - F_i\left(r_j-\frac{1}{2}\delta r\right)\right]dx$$

$$+ \frac{1}{A}\int_{r_j-(1/2)\delta r}^{r_j+(1/2)\delta r}\left[G_i\left(x_i+\frac{1}{2}\delta x\right) - G_i\left(x-\frac{1}{2}\delta x\right)\right]r\, dr$$

$$+ \frac{\delta_{i3}}{A}\int_{r_j-(1/2)\delta r}^{r_j+(1/2)\delta r}\int_{x_k-(1/2)\delta x}^{x_k+(1/2)\delta x} Hr\, dr\, dx \tag{A2}$$

where

$$A = \int_{r_j-(1/2)\delta r}^{r_j+(1/2)\delta r} \int_{x_k-(1/2)\delta x}^{x_k+(1/2)\delta x} r \, dr \, dx$$

$$= \frac{1}{2}\left[\left(r_j + \frac{1}{2}\delta r\right)^2 - \left(r_j - \frac{1}{2}\delta r\right)^2\right]\delta x \tag{A3}$$

The integrals in equations (A2) and (A3) are approximated by the trapezoidal rule. This constitutes a so-called "finite volume" approximation.

The f_i at a time t are first advanced inviscidly to a time $t + 1/2 \, \delta t$ at the cell centers ($r_j + 1/2 \, \delta r$, $x_k + 1/2 \, \delta x$), and then the inviscid flux densities, as computed at those points, combined with the viscous fluxes as computed at time t, are used to advance f_i to time $t + \delta t$.

Boundary conditions used are as follows. At the incoming boundary, where the flow is supersonic, all dependent variables are specified as desired. At the downstream (outflow) boundary, a zero gradient ($\partial f_i/\partial x = 0$) condition is used; this condition is also used on the top boundary (as $\partial f_i/\partial r = 0$) in the case of no outer wall. If there is an outer wall, slip boundary conditions are used ($v = 0$); on the body surface (and sting surface, if present), a no-slip, adiabatic condition is used.

REFERENCES

1. Weng, C. H.: Base Pressure Problems Associated with Supersonic Axisymmetric External Flow Configurations. Ph.D. thesis, Department of Mechanical and Industrial Engineering, University of Illinois, Urbana, Ill., 1975.

2. Weng, C. H.; and Chow, W. L.: Axiymmetric Supersonic Turbulent Base Pressures. AIAA J., vol. 16, no. 6, 1978, pp. 553–554.

3. Amsden, Anthony A.; and Harlow, Francis H.: Numerical Calculation of Supersonic Wake Flow. AIAA J., vol. 3, no. 11, 1965, pp. 2081–2086.

4. Allen, J. S.; and Cheng, S. I.: Numerical Solutions of the Compressible Navier-Stokes Equations for the Laminar Near Wake. Phys. Fluids, vol. 13, no. 1, 1970, pp. 37–52.

5. Kronzon, Y.; Rom, J.; and Seginer, A.: Laminar Supersonic Flow over a Backstep: An Numerical Solution at Higher Reynolds Numbers. Proceedings of 1976 Heat Transfer and Fluid Mechanics Institute, pp. 390–404.

6. Roshko, Anatol; and Lau, Jark C.: Some Observations on Transition and Reattachment of a Free Shear Layer in Incompressible Flow. Proceedings of 1965 Heat Transfer and Fluid Mechanics Institute, pp. 157–167.

7. Przirembel, C. E. G.; and Page, R. H.: Analysis of Axisymmetric Supersonic Turbulent Base Flow. Proceedings of 1968 Heat Transfer and Fluid Mechanics Institute, pp. 258–272.

8. Roshko, A.; and Thomke, G. J.: Observations of Turbulent Reattachment Behind an Axisymmetric Downstream-Facing Step in Supersonic Flow. AIAA J., vol. 4, no. 6, 1966, pp. 975–980.

9. Hama, Francis R.: Experimental Studies on the Lip Shock. AIAA J., vol. 6, no. 2, 1968, pp. 212–219.

10. Carpenter, P. W.; and Tabakoff, W.: Survey and Evaluation of Supersonic Base Flow Theories. NASA CR-97129, 1968.

11. Calarese, Wladimiro: Review of Methods of Solutions of Afterbody/Exhaust Nozzle Flow Fields. AFFDL-TR-74-108, Jan. 1974.

12. Moss, James N.: Flow-Field Analyses for Future Planetary Entry. Paper 79-098, AIAA Conference on Advance Technology for Future Space Systems, May 1979.

13. Engel, Carl D.: Jovian Probe Wake Flow Field. NASA CR-159021, 1979.

14. Nestler, D. E.; and Brant, D. N.: Development of an Afterbody Radiative and Convective Heating Code for Outer Planet Probes. Paper 78-862, 2nd AIAA/ASME Thermophysics and Heat Transfer Conference, May 1978.

15. Shirai, H.; and Park, C.: Experimental Studies of Radiative Base Heating of a Jovian Entry Model. Paper 79-0038, 17th Aerospace Sciences Meeting, Jan. 1979.

16. Park, C.: Modeling of Radiative Heating of Base Region of Jovian Entry Probe. Paper 79-0039, 17th AIAA Aerospace Sciences Meeting, Jan. 1979.

17. Stephenson, Jack D.: Measurement of Optical Radiation from the Wake of Ablating Blunt Bodies in Flight at Speeds up to 10 km per Second. NASA TN D-2760, 1965.

18. Mirels, H.: Estimate of Turbulent Boundary Layer Behind a Shock Wave Moving with Uniform Velocity. Report SAMSO-TR-77-166, The Aerospace Corp., Dec. 1977.

19. Launder, B. E.; and Spalding, D. B.: Lectures in Mathematical Models of Turbulence. Academic Press, London and New York, 1972.

20. Wray, A. A.: Computer Codes (to be published).

21. Cook, William J.; Chaney, Michael J.; Presley, Leroy L.; and Chapman, Gary T.: Application of Shock Tubes to Transonic Airfoil Testing at High Reynolds Number. NASA TP-1268, 1978.

22. Amsden, Anthony A.; and Harlow, Francis H.: Numerical Calculation of Supersonic Wake Flow. AIAA J., vol. 3, no. 11, 1965, pp. 2081-2086.

23. Tyler, L. D.; and Zumwalt, G. W.: Numerical Solution of the Flow Fields Produced by a Shock Wave Emerging into a Crossflow. Proceedings of 1966 Heat Transfer and Fluid Mechanics Institute, 1966, pp. 335-350.

24. Bloor, M. I.; and Evans, R. A.: Use of Vortex Discretization in Establishing Weak Shock Diffraction Patterns. AIAA J., vol. 17, no. 10, 1979, pp. 1046-1049.

25. Rakich, John V.; Vigneron, Yvon C.; and Tannehill, John C.: Navier-Stokes Calculations for Laminar and Turbulent Hypersonic Flow over Indented Nosetips. Paper 78-260, AIAA 16th Aerospace Sciences Meeting, Jan. 1978.

26. Pulliam, T. H.; and Steger; J. L.: On Implicit Finite-Difference Simulations of Three Dimensional Flow. Paper 78-10, AIAA 16th Aerospace Sciences Meeting, Jan. 1978.

1. Report No. NASA TP-1769	2. Government Accession No.	3. Recipient's Catalog No.
4. Title and Subtitle STEADY AND NONSTEADY SUPERSONIC TURBULENT AFTERBODY FLOW		5. Report Date February 1981
		6. Performing Organization Code
7. Author(s) Kenneth K. Yoshikawa and Alan A. Wray		8. Performing Organization Report No. A-8271
9. Performing Organization Name and Address NASA-Ames Research Center Moffett Field, California 94035		10. Work Unit No. 506-51-21
		11. Contract or Grant No.
12. Sponsoring Agency Name and Address National Aeronautics and Space Administration Washington, D.C. 20546		13. Type of Report and Period Covered Technical Paper
		14. Sponsoring Agency Code

15. Supplementary Notes

16. Abstract

A theoretical study of a supersonic turbulent afterbody flow field, containing regions of separation, recompression, recirculation, redevelopment, and inviscid flow, is made for axisymmetric supersonic steady and nonsteady flow past a cylindrical base supported by a sting.

The effect of the specific heat ratio γ of the incoming ideal gas on the flow properties, especially on pressure distributions along the base and sting surfaces and on reattachment distance, is investigated. The specific heat ratios considered are $\gamma = 1.2$, 1.4, and 1.667. Also, effects of other major parameters, such as eddy-viscosity coefficient (or effective Reynolds number) and Mach number, on the afterbody pressure and reattachment distance are studied and discussed. Evolution of shock-induced flow and stabilization time are examined and discussed for a transient problem.

The important influence of the flow-field geometry, pressure distributions, and reattachment distance on the aerodynamics radiative heat transfer for an atmosphere entry probe in high-speed flight are briefly described.

17. Key Words (Suggested by Author(s)) Afterbody flow, Turbulent wake flow, Recirculation flow, Shock tube flow, Separation Flow, Shock wave, Nonsteady flow, Blast wave, Axisymmetric supersonic flow	18. Distribution Statement Unclassified – Unlimited Subject Category 02
19. Security Classif. (of this report) Unclassified	20. Security Classif. (of this page) Unclassified

19. Security Classif. (of this report)	20. Security Classif. (of this page)	21. No. of Pages	22. Price*
Unclassified	Unclassified	23	A02

National Aeronautics and
Space Administration

Washington, D.C.
20546

Official Business
Penalty for Private Use, $300

THIRD-CLASS BULK RATE

NASA

POSTMASTER: **If Undeliverable (Section 158
Postal Manual) Do Not Return**